Study of light neutron-deficient nuclei

Progress report

Erik Asbjørn Mikkelsen Jensen

Supervisors: Karsten Riisager & Hans Fynbo

July 21st 2021

1 Introduction

In the whole rich nuclear world of various compositions of neutrons and protons – the two types of nucleons – there are believed to be somewhere between roughly six thousand and nine thousand unique combinations forming what we refer to as *nuclides*. Out of this lot, a bit more than three thousand nuclides have been observed up to this date, and only a few more than 250 of these nuclides are stable [1]. This fraction of stable nuclides forms the so-called *valley of stability* in the chart of nuclides, a slice of which is depicted in figure 1.1; all other nuclides spontaneously decay in one way or another, eventually becoming stable nuclides themselves. In addition to this distinction between *nuclides*, each individual nuclide also has one or more configurations of their constiuent *nucleons*, and all of these configurations possess different energies and quantum properties relative to one another, forming what we refer to as *nuclear structure*. How can we probe the nuclear structure of unstable nuclides? One possibility is by exploiting the process of β-delayed particle emission.

The plan of my PhD project, as it was originally formulated, is to study the β-delayed particle emission of the nuclides ^{22}Al, ^{26}P, ^{23}Si and ^{27}S by carrying out two separate new experiments, with the first experiment focusing on the two former nuclides and the second experiment focusing on the two latter nuclides. The experiments are to be carried out at Michigan State University (MSU) in the United States of America. The COVID-19 situation has, however, hampered this plan somewhat, as I and the rest of the Subatomic

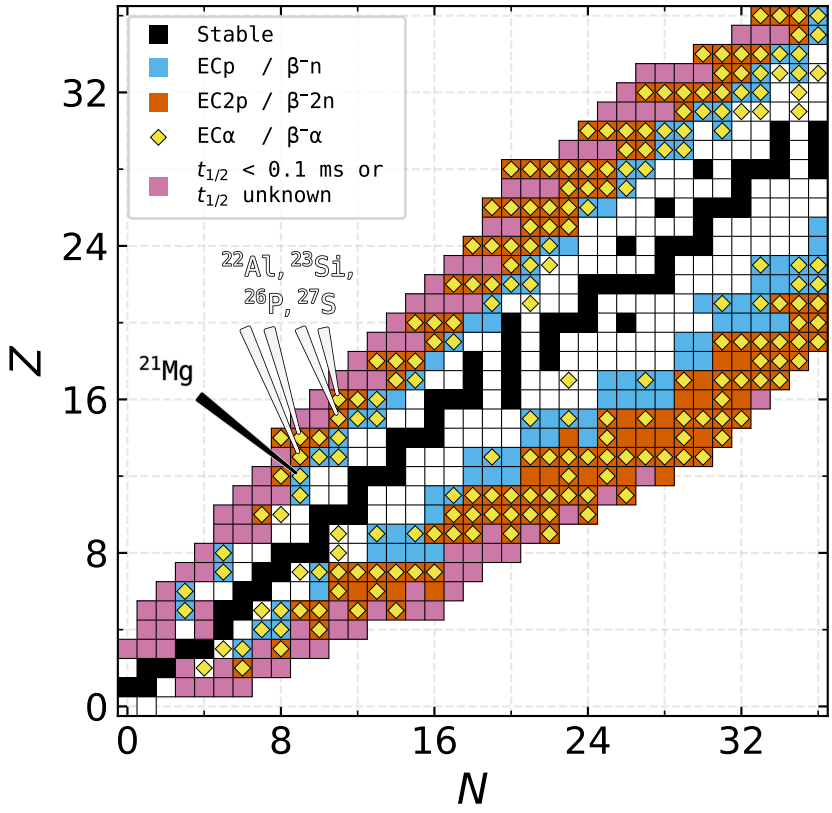

Figure 1.1: Onset of select kinematically possible beta-delayed decays for light nuclides. The possibility of beta-delayed 2-nucleon emission implies the possibility of beta-delayed 1-nucleon emission. The five highlighted nuclides are the neutron-deficient nuclides I either have studied or plan to study. The figure was created by utilising the publicly available tool NUCHART [2] (made by me) which extracts nuclear masses, reaction energies and decay properties from the AME2016 [3, 4] and NUBASE2016 [5] data files available at AMDC's website [6].

Group (my supervisors, a fellow PhD student and our European collaborators) were supposed to carry out the first of these experiments in the autumn of 2020 at the National Superconducting Cyclotron Laboratory (NSCL) at MSU; this unfortunately became impossible. We are, however, still hopeful of being able to carry out perhaps just the first of the two experiments within a time frame which will reasonably allow me to analyse the resulting data and present it before my PhD is finished.

At MSU, during the worldwide lockdown, work towards the commis-

sioning of the Facility for Rare Isotope Beams (FRIB) has carried steadily on, and the first experiments at FRIB are planned to take place before the end of the year. For our experiment on ^{22}Al and ^{26}P, for example, the upgrade from NSCL to FRIB entails at least a factor 10^3 increase in yield [7] – all the more reason to grab the first opportunity to complete these experiments! The main themes of both experiments are: (1) the exploration of the mechanism by which the β-decay products undergo multi-proton or alpha emission, (2) the mapping of the β-decay strength to the decay products, and (3) the study of resonances above the proton separation energies of the decay products.

In the following sections I will first give an overview of the necessary theory behind β-delayed particle emission. I will then describe the experimental methods involved in experiments on these kinds of nuclei and, specifically, I will motivate the utilisation of MSU's beam facility and the experimental kit to be used there. Following that, I will describe the process of going from raw data to analysable data, introducing some particle identification methods along the way. A section is then devoted to describing some of the more extensive software development I have carried out to facilitate my own and the Subatomic Group's analyses. Finally, I will present some preliminary results of my data analysis of a subset of data from an experiment carried out at the ISOLDE Decay Station (IDS) at CERN in 2015; this data analysis has the potential to provide new insight into the β-delayed particle emission of ^{21}Mg, and the analysis also serves to prepare me for the analyses of the new data from MSU to come.

2 β-delayed particle emission

If we pick any stable isotope in the chart of nuclides and then strip away one neutron at a time, we will, at each step, move further and further away from the valley of stability. Eventually we reach the *proton drip line*, where the protons simply drip off, as the resulting composition of nucleons is completely unbound. Of course, instability of the isotopes kicks in long before we reach the drip line, and the further away we are from the valley of stability, the shorter the lifetimes of the isotopes. The same idea holds for stripping

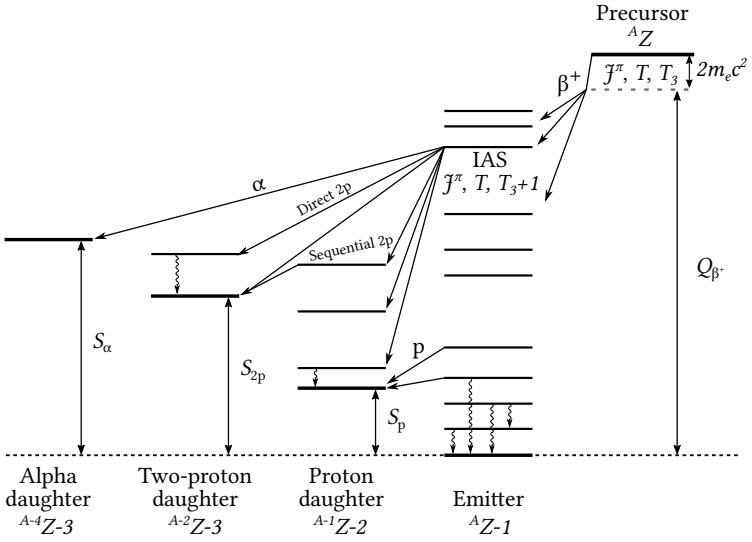

Figure 2.1: Schematic representation of β^+-delayed particle emission. Figure inspired by figure 3 in [8].

away protons from a given stable isotone, eventually reaching the *neutron drip line*; we either move straight to the left or straight downwards in figure 1.1 from a given starting point.

The practical problem of short lifetimes is what makes β-delayed particle emission an attractive means of studying the, otherwise elusive, neutron- and proton-deficient nuclei. β-decay is a relatively slow process (of order 10-100 milliseconds for the nuclides of interest to my project), and it is today quite possible, within typical β-decay lifetimes, to prepare radioactive beams and guide them towards a detection setup where the decay and subsequent particle emission of the stopped beam particles can be observed [8, 9]. The available radioactive beams can have neutron-to-proton ratios substantially different from the corresponding stable isobars. For the most unstable nuclides closest to the drip lines, however, particle emission from the ground-state dominates β-decay, and this method of investigation falls short. Still, referring again to figure 1.1, the richness of probes of exotic nuclear structure at our disposal using this method should not be disparaged.

Focusing for now on the neutron-deficient (or proton-rich) side of the chart of nuclides, a typical decay scheme (with well-separated energy levels for light nuclides) might look as depicted in figure 2.1. The *precursor* decays

into the *emitter* via a β^+ or electron capture process, especially populating the Isobaric Analogue State (IAS), the transition to which preserves spin, parity and isospin $\mathcal{J}, \pi, T$ whilst changing the projection of isospin T_3 by one due to the conversion of a proton into a neutron. The Q-value of the decay of the precursor less the proton, two-proton and α separation energies $S_\mathrm{p}, S_\mathrm{2p}, S_\alpha$ of the emitter to the *particle daughters* dictates whether it is kinematically possible for subsequent particle emission to occur. It is perhaps worth emphasising that the term β-delayed particle emission is quite apt, as the particle emission (including the emission of photons) occurs more or less instantly after the β-decay of the precursor; the particle emission of the emitter is indeed delayed by the lifetime of the precursor.

When we speak of the β^+-delayed particle emission of a nuclide ${}^A Z$, the object of main interest is really the nuclide ${}^A Z\text{-}1$ — the emitter. The rich number of open decay channels, due to the large Q-value and the imbalance of neutrons and protons, offers great insight into the nuclear structure of the emitter by observation of the emitted charged particles and photons. Despite the emitter being the object of main interest, the amount of detail in which we can investigate the emitter within a limited time frame is dictated by the intensity of the β transition from the precursor via the familiar ft expression [10, chap. 9],

$$ft = \frac{K}{{g_\mathrm{V}}^2 B_\mathrm{F} + {g_\mathrm{A}}^2 B_\mathrm{GT}}; \quad K = \frac{2\pi^3 \hbar^7 \ln 2}{{m_\mathrm{e}}^5 c^4} \tag{2.1}$$

with g_V and g_A representing the vector and axial vector coupling strengths of the Fermi and Gamow-Teller type β decays respectively and with $B_\mathrm{F} \propto \left|\langle f \left|\tau\right| i\rangle\right|^2$ and $B_\mathrm{GT} \propto \left|\langle f \left|\tau\sigma\right| i\rangle\right|^2$ being the matrix elements from the initial state i to the final state f under the influence of the isospin and spin operators τ and σ in the Fermi and Gamow-Teller type transitions. The β strength is a core component in the comparison of theory and experiment.

3 Experimental approach

In this section I will describe our experimental approach both in general terms and specifically in relation to the experiments to be carried out at

MSU. The charged particle detectors which we employ in-house, at the department in Århus, complement the capabilities of many worldwide facilities very well, and as such our charged particle detectors are virtually always with us when we go abroad to utilise our beam times. Typically, we can aid the various facilities with regards to compact charged particle detection setups, whilst they can aid us with gamma ray detection and exotic particle production.

3.1 Production of exotic nuclei

Historically, the decay experiments carried out by the Subatomic Group have mainly taken place at the ISOLDE facility at CERN and the IGISOL facility at the University of Jyväskylä. These facilities exploit the so-called *ISOL* (Isotope Separation On-Line) method which can provide beams of exotic nuclei of high purity given the facilities' large mass-separation resolutions. In the ISOL method a relatively thick target is irradiated by a primary beam, resulting in the diffusion of various unstable nuclides from the target surface. The nuclides are then guided to an ion source, from which some of them are selectively emitted to form the secondary low-energy beam (typically ~50 keV). The beam is mass-separated and can then be guided towards a stopping medium in which the desired unstable nuclides decay, allowing for the observation of their decay products.

The *in-flight* method is the ISOL method's counterpart for producing beams of exotic nuclei. In this method the higher energy primary beam is incident on a relatively thin target, resulting in the emergence of fragmentation products with virtually the same velocity on the other side of the target. The fragmentation products are then mass-separated and guided towards a detection unit, in a manner similar to the ISOL case. Some of the in-flight method's advantages over the ISOL method are shorter separation times and larger separation efficiencies due to the smaller significance of the primary target's chemical properties [9]. The larger energy spread of the fragmentation products does, however, generally result in beams of lower purity as compared to the ISOL method.

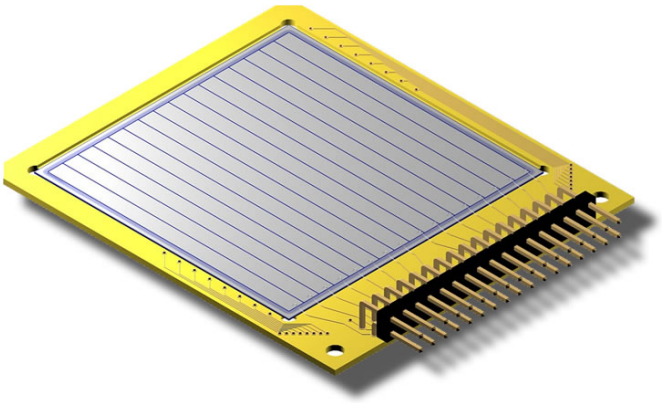

Figure 3.1: Double-sided silicon strip detector from Micron Semiconductor Ltd [12]. Here the front side is shown with its 16 vertical strip segments.

The radioactive beam facility at MSU rectifies this shortcoming by following the fragment separation with thermalisation in a gas cell. This reallows high-precision mass-separation, and the quality of the radioactive beams can be "brought back" towards ISOL levels at a relatively small cost of separation times and efficiencies, maintaining its superiority in these latter aspects as compared to the ISOL method (see e.g. [11, chap. 3]).

For the precursors ^{22}Al, ^{26}P, ^{23}Si and ^{27}S with half-lives around 90 milliseconds down towards 15 milliseconds [5], the shorter separation times have a large impact on the comparative yields. This is crucial to the proper characterisation (or even identification) of multi-proton and alpha emission from the precursors' corresponding emitters. The statistics on these decay branches have been quite limited in the studies previously carried out [8], and the experiments to be carried out at MSU should be able to improve these statistics by several orders of magnitude. By extension, this also allows a more complete mapping of the strength of β-decay and the resonances above the proton separation energies in the daughter nuclei. In other words, we seek to meet the goals outlined in the introduction by virtue of much greater statistics, and equally by virtue of our particle detection capabilities, which is the topic of the next subsection.

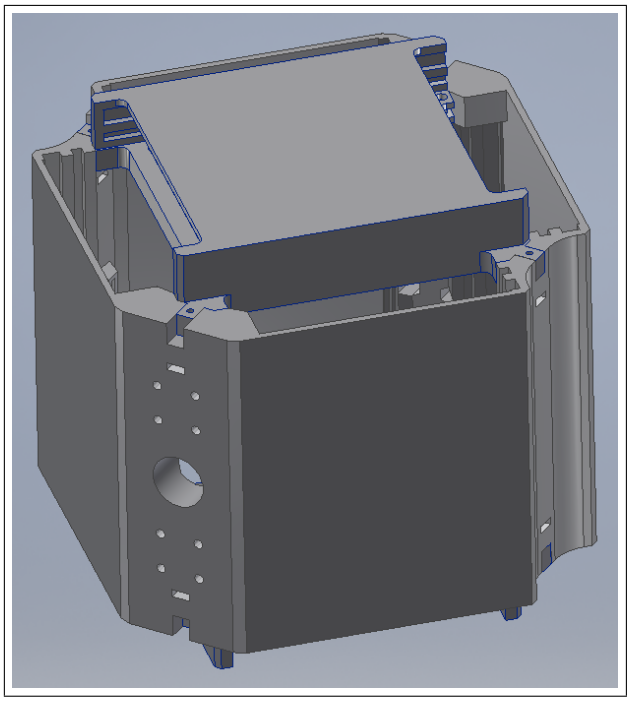

Figure 3.2: Specially designed cube which is to hold a total of 12 charged particle detectors during the experiments at MSU. At the top of the left-facing side, for instance, two slits, each of which are to hold a detector, can be seen.

3.2 Particle detection

The working horses of our experimental kit in Århus are our large-area silicon detectors from Micron Semiconductor Ltd. Out of the options from their catalogue [12], we especially employ their *W1* design (a detector of this design is shown in figure 3.1) and their *MSX25* design. The latter of these designs shares its dimensions with the former and is merely a slab of silicon with an active surface area measuring 50.0×50.0 mm^2, its thickness ranging from 40 µm up to 1500 µm; this type of detector is commonly referred to as a *Pad detector* or a *single-sided silicon detector* (SSSD). The former design, the W1 design, has the entire slab of silicon divided into 16 *vertical* silicon strip segments on the front side and 16 *horizontal* silicon strip segments on the back side; the overlap of the 32 strips defines 256 individual silicon detector pixels in these *double-sided silicon strip detectors* (DSSSDs). The ultra-thin dead layers of around 100 nm and the minute 2% metal coverage (to allow

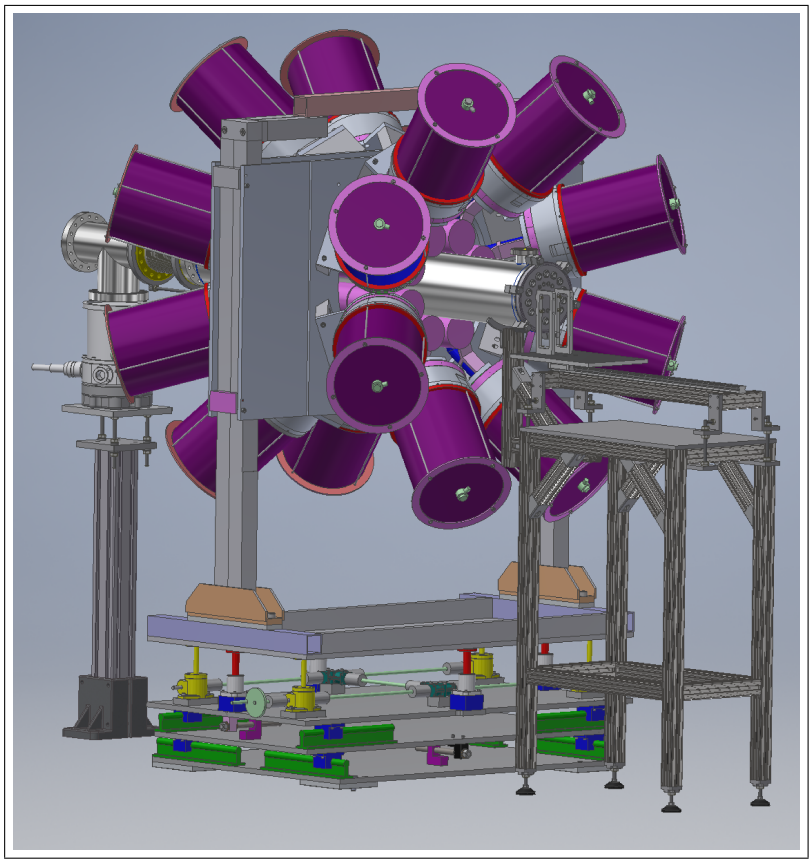

Figure 3.3: Technical drawing of the entire setup to be used at the stopped beam area at MSU. The purple cylinders are the gamma detectors of the SeGA at MSU. These are all pointing at the cube of figure 3.2, which is situated inside the long aluminium tube.

for signal readout) on the front side [13] make these detectors particularly well-suited for the detection of light charged particles.

For the experiments to be carried out at MSU we plan to surround the source of decaying nuclides with six DSSSDs on the inside of the specially designed cube shown in figure 3.2. Just behind each of these six detectors a Pad detector will also be situated. The detector in front will have a relatively small thickness, and the other detector will have a relatively large thickness; the usefulness of this will be demonstrated in section 4.2. Right at the centre of the cube in figure 3.2, a thin collection foil will be situated. The low-energy radioactive beam will be incident on the hole in the middle of the cube from the outside, and the beam particles will then be completely stopped in the

collection foil, allowing for their decay. The positioning of the detectors relative to the collection foil provides a solid angle coverage of 54%.

With the detection of charged particles under control due to our own compact silicon detector cube, the photons, which are also emitted after the decay of the precursor, still remain. The detection of these photons can provide invaluable extra insight, if observed in coincidence with one or more charged particles ejected from the emitter. For the experiments to be carried out at MSU, we intend to utilise the Segmented Germanium Array (SeGA) available at the facility [14] in the so-called *betaSeGA configuration*. The SeGA consists of 16 high-purity large volume germanium detectors, each of which consists of 32 individual segments. These detectors will be placed right outside the vacuum chamber (a long aluminium tube which was manufactured in Germany and shipped to us in Århus), pointing at the collection foil, which is situated inside the chamber in the detector cube. A technical drawing of the entire setup is shown in figure 3.3.

3.3 Data acquisition system

When we bring our detectors to an experiment, we also have to bring our entire data acquisition system (abbr. "DAQ"), as it is tailor-made for the proper operation of our detectors and for the eventual proper recording of the vastly multichannel (160-220 individual energy channels is common) data detected by our setup. A schematic representation of our DAQ is shown in figure 3.4. Each detector, situated close to the reaction or decay products of interest, has its own preamplifier as close by as possible. The preamplifiers deliver the necessary bias to the detectors and convert the short current pulses from the detectors to long, sharply peaked and amplified voltages. The preamplifiers are as close to the detectors as possible to reduce noise pickup on the signals from the detectors which carry currents of order picocoulomb. The outputs of the preamplifiers are then further amplified and shaped into Weibull distribution-looking signals in the shaping amplifiers and delivered to the analog-to-digital converters (ADCs) of the DAQ, in which the voltage peaks of the analog signals are converted into binary numbers (also referred to as channel numbers). Along the entire signal chain, the amplitudes are

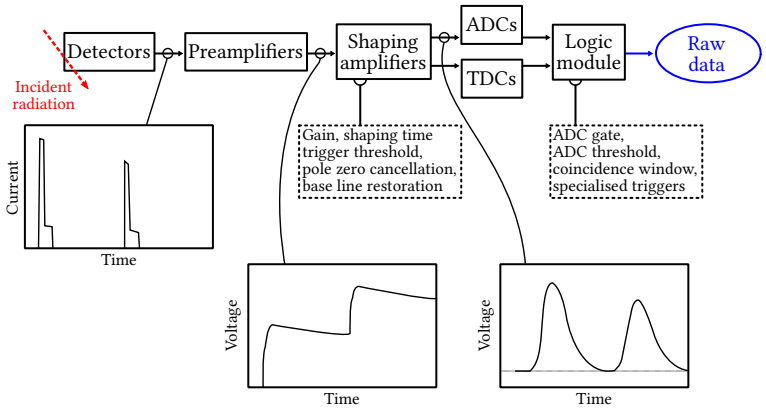

Figure 3.4: Schematic representation of our data acquisition system. At the centre left and along the bottom of the figure are visualisations of some signals as they progress through the system; the time scales of the different graphs are *not* equatable. The dashed boxes contain some of the parameters we can adjust on the individual modules.

sought as proportional as possible to the energies originally deposited by the radiation incident on the detectors.

Our DAQ stands a bit out by the fact that the shaping amplifiers also provide the timing signals for the time-to-digital converters (TDCs). The shaping amplifiers provide sharply changing logical pulses, indicating the time of arrival of each energy signal, and the arrival of these pulses in the TDCs are in turn converted to binary numbers. Finally, at the logic module we decide on the specific combination of input signals which might be indicative of a nuclear reaction of interest (the label *specialised triggers* in figure 3.4) to a given experiment. When the conditions of the logic module are met, the ADC and TDC values of relevance are recorded in a raw data format.

4 Data analysis

In this section I will introduce our data analysis software and provide some preliminary insights into constraining our vastly multidimensional data sets.

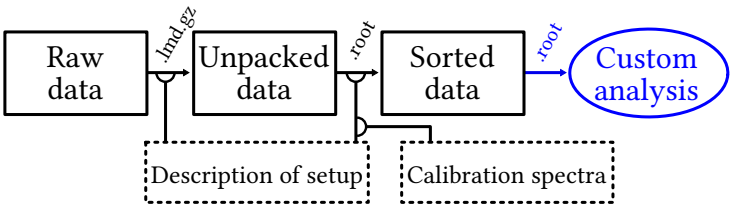

Figure 4.1: Flowchart representation of the AUSAlib pipeline. By providing the description of a given setup and corresponding calibration spectra, the raw data are converted from a binary list mode format to a custom format utilising ROOT's tree description.

4.1 Software

AUSAlib (**A**arhus **U**niversity **S**ub**A**tomic **lib**rary) was pioneered in-house by (at the time) postdoc Oliver S. Kirsebom and PhD students Michael K. Munch and Jesper H. Jensen in the 2010s. The analyses of the experiments carried out in the Subatomic Group have many aspects in common, but until the advent of AUSAlib these aspects were always more or less implemented anew in each analysis due to the limited configurability of the specialised analysis made for each preceding experiment. AUSAlib is a publicly available [15] C++ framework based on ROOT, a vast nuclear and particle physics framework developed and maintained by a sizeable team at CERN [16].

In brief, AUSAlib facilitates the analysis of our type of experiments by providing a framework in which the user specifies their

- Setup – i.e. the detectors used in a given experiment, including their individual types, their specific dimensions and their positions and orientations with respect to the target
- Calibration spectra – these spectra are obtained in the same manner as any real measurement (figure 3.4) and should also be accompanied by a specification of the energies and intensities of the calibration source

By providing this information, AUSAlib converts the raw data, introduced earlier, into "unpacked" and then into "sorted" data files as outlined in figure 4.1, leading the user more swiftly to the specific physics analysis of the data.

In the "sorting step", apart from applying the calibrations to the data, the hitherto independent hits recorded in the front and back channels of the double-sided detectors are matched in a way that minimises the absolute energy difference $|E_{\text{front}} - E_{\text{back}}|$ (and optionally discards hits with too large differences) for the various hits recorded for each event. As a result, the energies, timings *and* directions of the particles which hit any of the double-sided detectors of the setup are known at this point.

These are the main steps in going from raw to analysable data, but AUSAlib can also aid specifically in the analysis of the data, as it provides interfaces for the user to specify how each event, generally containing several hits distributed in the different detector channels, should be handled in order to carry out the user's specific analysis. On top of this, AUSAlib also comes with tabulated mass values, stopping power tables, range tables and more. This enables the user, for example, to correct for the energy loss of a certain particle in the effective dead layer thickness of a given detector by writing a single line of code, provided that AUSAlib has the description of the setup.

Despite the original authors no longer being directly affiliated with the Subatomic Group, AUSAlib is still in active use (even by graduate and undergraduate students at the Department of Physics and Astronomy) and, more importantly, in active development. Andreas Gad, another PhD student in the Subatomic Group, and I are continuously maintaining and expanding AUSAlib as required by the data analysis needs of both ourselves and others. In particular, I have committed a significant amount of work during the spring of 2021 into future-proofing and maintaining AUSAlib. I will describe this work in section 5.

4.2 Particle identification

As particles penetrate a given medium, they experience an infinitesimal change in energy $\mathrm{d}E$ per infinitesimal distance $\mathrm{d}x$ traversed in the medium. The stopping power S is, in these terms, defined as

$$S(E) = -\frac{\mathrm{d}E}{\mathrm{d}x} \tag{4.1}$$

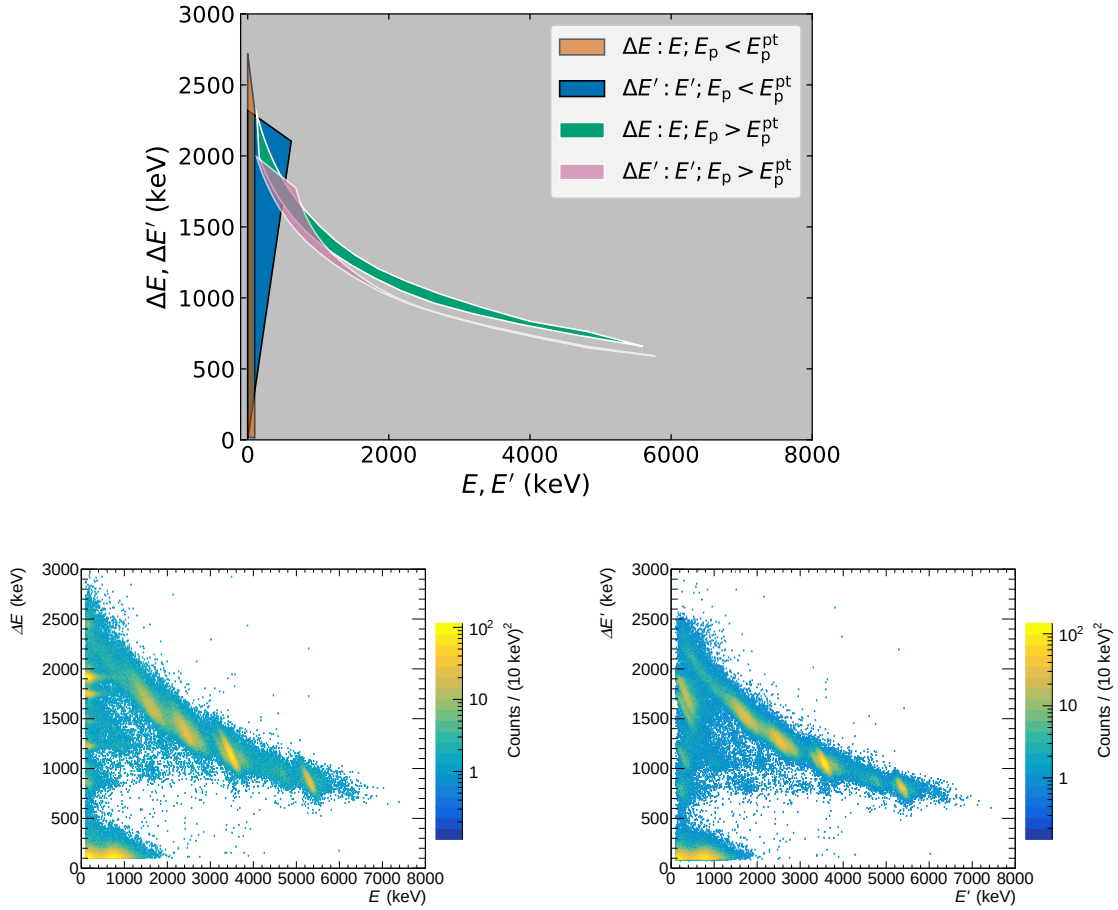

Figure 4.2: Identification of protons in a detector telescope. The top figure shows curves of ΔE vs. E and $\Delta E'$ vs. E' (see text) made from tabulated stopping power tables. The orange filled area has artificially been made 100 keV wide in place of its actual width of 0 keV, and the green and magenta areas continue all the way up to 8-10 MeV, but they become too thin to be depicted above 6 MeV. The two bottom figures show real data from the same setup; here the detectors have finite resolutions, there are chance coincidences, and there are large "noise" contributions in the lower left corners.

with the minus sign in the definition making stopping power an intrinsically positive quantity. Stopping power depends on the type of particle and its energy E (the latter explicitly noted in the above definition) as well as the type of medium through which the particle travels. Each type of particle has its own characteristic range of stopping powers in various media, and we can exploit this fact in the analyses of our data.

One way of exploiting this phenomenon is by arranging our detectors

in a so-called *telescope configuration*. If a particle incident on a detector is of sufficiently low energy as compared to the distance it has to traverse in the detector, it will be completely stopped in the detector and deposit all of its energy there. On the other hand, if the particle's *range* in the detector is greater than the distance is has to traverse in the detector, it will *punch through* the detector, having only lost a fraction of its energy. By placing another detector behind the first detector, thus constructing our *telescope*, and by cleverly choosing different combinations of detector thicknesses, we can selectively stop different types of particles of certain energy ranges in the different detectors.

These telescope configurations may consist of an arbitrarily large number of detectors, but in our experimental setups we generally have a thin detector located closest to the source of particle emission and then a thick detector placed right behind it. The thin detector is generally referred to as the ΔE *detector*, and the thick detector is referred to as the E *detector*. An example of the possible energy depositions of protons in a 60 µm ΔE detector and a 500 µm E detector is shown in figure 4.2. When the proton energies E_p are less than the energy necessary for the protons to punch through the ΔE detector, E_p^pt, all of their energies are solely deposited in the ΔE detector. With proton energies above this threshold the proton energies are distributed amongst the ΔE and E detectors (until E_p becomes so large that protons also punch through the E detector).

A correction to the deposited energies ΔE and E, essentially integrating equation 4.1 over the effective thickness of the thin detector whilst treating the integrand as a constant, is

$$\Delta E' = \Delta E \cos\theta \tag{4.2}$$

$$E' = E + (1 - \cos\theta)\Delta E \tag{4.3}$$

with θ being the angle of incidence of the particle with respect to the detector surface. These quantities are also depicted in figure 4.2 for the same scenario, and, as can be seen, these quantities serve to flatten the area covered by ΔE vs. E when $E_\mathrm{p} > E_\mathrm{p}^\mathrm{pt}$. This correction is useful for the distinction between particles of relatively similar stopping powers, i.e. close-lying

ΔE vs. E curves. As can also be perceived from the real data in figure 4.2, the resolutions of our detectors are, however, of key importance in minimising the overlap of ΔE vs. E curves of different types of particles.

Apart from selectively detecting particles by using our knowledge of their stopping powers, we also need to correct for the particles' energy losses in the effective thicknesses of the inactive layers of our detectors, in our target foils and the like; this is very easily done with the aid of AUSAlib and its stopping power tables.

5 Software development and maintenance

As I mentioned at the end of section 4.1, I have put a significant amount of effort into maintaining and expanding upon our software libraries during the spring of this year. AUSAlib and its related data analysis tools are built from the ground up with a substantial amount of thought put into their architecture, but their development have also proceeded in an *ad hoc* manner, as is only natural in a scientific (i.e. iterative) environment. As such, I have had to expand upon the parsing of detector configurations in AUSAlib during my data analysis work.

Usually, for a telescope configuration, we let a double-sided detector be the ΔE detector whilst a single-sided detector takes the role of the E detector, but in the experiment on ^{21}Mg at the IDS in 2015, there happened to be a configuration with the roles reversed; prior to my extensions, AUSAlib could not properly accommodate this type of configuration. The Clover detectors used during the experiment also needed to be implemented. These tasks were relatively small, but as I implemented these expansions of AUSAlib, it became clear to me that AUSAlib was in pressing need of some structural maintenance.

ROOT, which AUSAlib is based on, will upgrade from the C++11 standard to the C++14 standard, when ROOT version 7 is eventually released [17], and support for version 2.8 of CMake [18], which AUSAlib was originally designed for, will be dropped by systems in general as they start providing newer versions of CMake, which has deprecated the use of version 2.8 since

```
cmake_minimum_required(VERSION 2.8)
project(my_analysis)

set(CMAKE_MODULE_PATH "${CMAKE_MODULE_PATH};${CMAKE_SOURCE_DIR}/cmake")
set(CMAKE_CXX_FLAGS "${CMAKE_CXX_FLAGS} -std=c++11")
set(LIBRARIES "")

find_package(AUSALIB REQUIRED)
include_directories(${AUSALIB_INCLUDES})
list(APPEND LIBRARIES ${AUSALIB_LIBRARIES})
find_package(ROOT REQUIRED)
include_directories(${ROOT_INCLUDE_DIR})
link_directories(${ROOT_LIBRARY_DIR})
list(APPEND LIBRARIES ${ROOT_LIBRARIES} Spectrum MathMore)
find_package(CURL)
if (CURL_FOUND)
  include_directories(${CURL_INCLUDE_DIRS})
  list(APPEND LIBRARIES ${CURL_LIBRARIES})
  add_definitions("-DAUSA_HAS_LIBCURL")
endif(CURL_FOUND)

link_libraries(${LIBRARIES})
add_executable(main_analysis main.cpp)
```

```
cmake_minimum_required(VERSION 3.15)
project(my_analysis)

find_package(AUSALIB REQUIRED)

add_executable(main_analysis main.cpp)
target_link_libraries(main_analysis PRIVATE AUSA::AUSA)
```

Figure 5.1: Example of a project's CMake specifications utilising the old (left) and new (right) version of AUSAlib. The new version of AUSAlib provides its own dependencies, so statements like FIND_PACKAGE(ROOT) and FIND_PACKAGE(CURL) are no longer necessary.

CMake version 3.19 [19]. Since ROOT also uses CMake for build system generation, AUSAlib is quite reliant on its continuing functionality.

Apart from the necessity for AUSAlib to eventually comply with these upgrades, there are also many benefits to be gained from these newer programming language and build generation standards. The upgrade to the C++ 14 standard allows our software to rely on fewer obscure libraries and utilise instead mainly the C++ standard library. I have also been able to completely remove some arcane and ambiguous hacks in our software due to this upgrade. This makes AUSAlib more robust moving forward.

The top act of my software development thus far is, however, the upgrade of our CMake specifications to comply with version 3.15 and above. CMake version 3.15 can reasonably be expected to be provided by most active Linux distributions at the time of writing [20] and it has sufficiently many features which allow the CMake developer to focus on describing the software and its dependencies instead of worrying about the finer build system details. An example of a result of my upgrade of AUSAlib's CMake specifications is shown in figure 5.1, which depicts the greater ease of incorporating AUSAlib in an example project called *my_analysis*; not only is the newer version of AUSAlib more easily available to the user, it is also much more robust, as AUSAlib's *CMake targets* are now exported properly (the meaning and ra-

tionale of this is detailed in ref. [21]).

Apart from this result of the upgrade, my focus has primarily been on AUSAlib's future maintainability. My consolidation of AUSAlib's CMake specifications should entail only very minor upgrades of the specifications in the future. Speaking in favour of this statement is the fact that the development team behind CMake adopted a markedly different design philosphy in regards to build system generation with CMake version 3 (necessitating the major overhaul of AUSAlib's CMake specifications in the first place), but the change in CMake's design philosophy was brought about exactly due to the lack of maintainability of the older versions of CMake and, by extension, of all software libraries utilising CMake – CMake version 3 is itself immensely more future-proof, and so AUSAlib should be as well. I have taken much inspiration from references [21] and [22] in my work with CMake. My upgrade of AUSAlib is available at Aarhus University's GitLab server [23], and it will be merged with the main AUSAlib repository as soon as our continuous integration systems are properly prepared for it.

The eventual full release of ROOT version 7, which will entail yet another overhaul of AUSAlib, still remains. However, the ROOT Team are gradually including experimental ROOT 7 features in their more recent releases, as they are being developed. In parallel with upgrading the CMake and C++ standards of AUSAlib, I have also accommodated some of the changes included in these newer releases. I expect to continue this sort of work as the ROOT Team progresses in their development and, as such, the change from ROOT version 6 to 7 in AUSAlib need not become one monumental task, but rather a gradual process.

6 Study of ^{21}Mg

As mentioned in the introduction, I have commenced analysing data from an experiment carried out at the ISOLDE Decay Station (IDS) at CERN back in 2015. The main attraction of the experiment at the time was actually the nuclide ^{20}Mg, and data on ^{21}Mg were obtained for calibration purposes. There is, however, as will become clear in the following, quite a lot of nuclear struc-

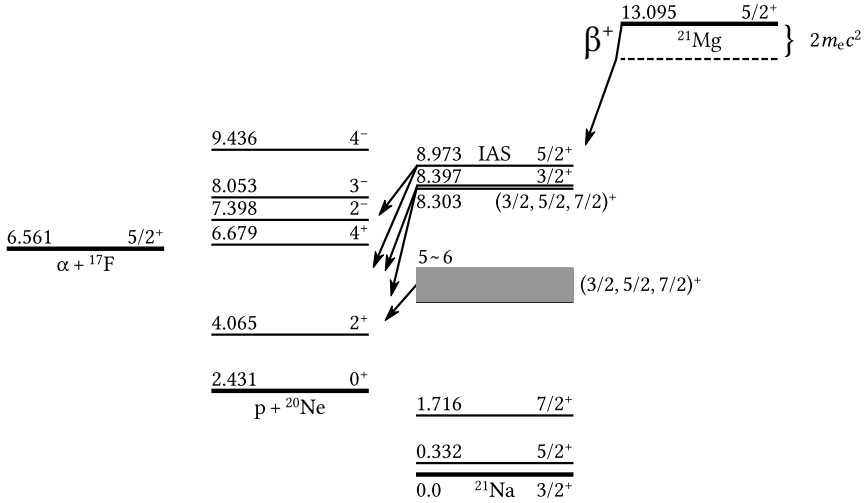

Figure 6.1: Selected states in the decay of ^{21}Mg with spins and parities of the states marked on the right and energies (in MeV) of the states relative to the ground state of ^{21}Na marked on the left.

ture of ^{21}Mg to be revealed from this subset of the experimental data.

Prior to my work, Morten V. Lund, a former PhD student in the Subatomic Group, studied the β-delayed decay of ^{21}Mg from an experiment carried out at the IDS in 2011 [24], utilising just a single W1–Pad detector telescope and a gas–silicon–silicon detector telescope. The experiment in 2015, in contrast, utilised four W1–Pad detector telescopes (ignoring a few details for now) and a single thick W1 detector; the potential insights to be gained on ^{21}Mg from this newer experiment are quite large due to the greater solid angle coverage, overall better energy resolution and, in fact, longer mesurement time on ^{21}Mg as compared to the experiment in 2011. Sofie T. Nielsen, a former Master's student in the Subatomic Group, took a first look at the newer ^{21}Mg data, focusing especially on the photons emitted in the β-delayed decays, and detailed her findings in her Master's thesis [25].

My plan is to expand on Morten's and Sofie's findings, starting from the ground up, as AUSAlib was not available for Morten to utilise, and its capabilities are much greater now compared to when Sofie did her research. Starting in this fashion, from a mostly clean slate, serves as an extra independent check of prior findings. Furthermore, the methods I will develop in

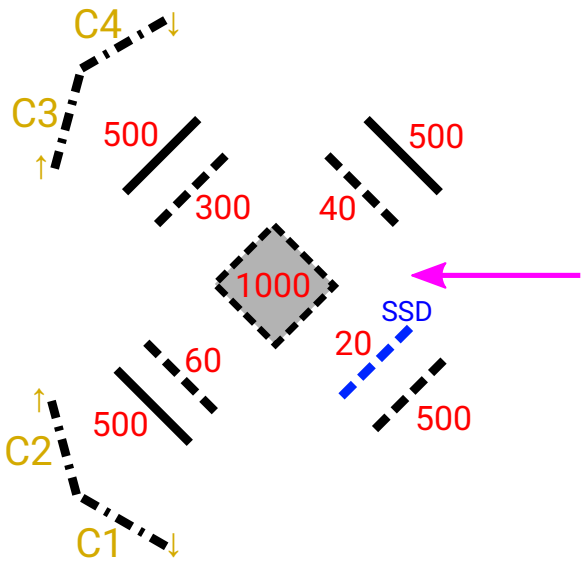

Figure 6.2: Schematic representation of the detection setup used during the experiment, seen from above. The beam comes in from the right, as indicated by the magenta arrow. Solid lines represent Pad detectors, dashed lines represent strip detectors and dash-dotted lines represent Clover detectors (C1-C4). The red numbers indicate active volume thicknesses of the silicon detectors in micrometers. The collection foil is located at the centre, above the 1000 µm thick detector. The dashed blue detector is a single-sided detector with 16 parallel strips on the front side, and all other strip detectors are double-sided.

the analysis of ^{21}Mg can be carried over more or less directly to the analysis of the experiments to be carried out at MSU; since we are somewhat behind schedule in terms of carrying out the newer experiments, it seems prudent to be ahead of schedule for the subsequent analyses of the experiments. Finally, there are many new features in the decay of ^{21}Mg to be observed already in my preliminary findings. The decay scheme of ^{21}Mg is shown in figure 6.1.

6.1 Constraining the data

The setup used during the experiment at the IDS is schematically depicted in figure 6.2. All silicon detectors are located in a vacuum chamber, facing a small collection foil at the centre of the chamber. A radioactive beam is allowed into the chamber and its beam particles are stopped in the collection foil. The *Clover detectors* (C1-C4 in the figure) are located just outside the

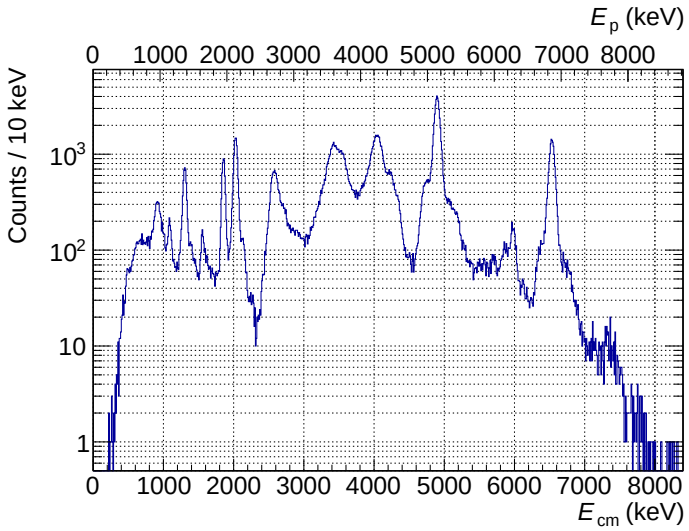

Figure 6.3: Combined proton spectrum from the 60 µm–500 µm and 40 µm–500 µm telescopes of figure 6.2.

vacuum chamber, facing the collection foil inside the chamber. These High Purity Germanium detectors available at the IDS (described in detail in [26, chap. 2]) are conceptually quite similar to the detectors of the SeGA at MSU. The 4 germanium detectors used during the experiment at the IDS are four-fold segmented, rather than thirty-two-fold segmented.

The setup utilised at the IDS grants many means of constraining the data, thus filtering out uninteresting events and revealing the nature of β-delayed particle emission in ^{21}Mg. Referring back to the bottom two plots in figure 4.2, we see chance coincidences and we see a β background in the lower left corners. These ΔE vs. E graphs do in fact contain all events recorded in the 60 µm–500 µm telescope (figure 6.2) from the runs with beams of ^{21}Mg. With guidance from the top plot in figure 4.2 it is possible to make *graphical cut*s, i.e. define areas of interest, filtering out the unwanted data outside these areas. A result of such graphical cuts (one area of ΔE vs. E with $E_p < E_p^{pt}$ and another area with $E_p > E_p^{pt}$ in the language of figure 4.2) is shown in figure 6.3. Without these graphical cuts the low-energy range of figure 6.3 would drown in background, and the intermediate-energy range (where ΔE vs. E for $E_p < E_p^{pt}$ and $E_p > E_p^{pt}$ overlap in figure 4.2) would yield questionable results. For events in the area where $E_p > E_p^{pt}$, the deposited energies in the

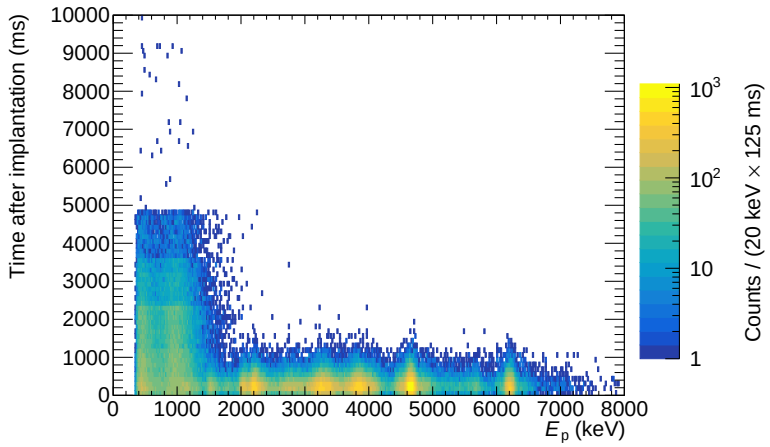

Figure 6.4: Time after start of production of ^{21}Mg at the production target against proton energies recorded in one of the telescopes of the setup.

two detectors are added, and all deposited energies are corrected for their energy losses due to their traversal of the various media within the setup.

Another feature from the experiment which can be exploited is the repetition cycle of the Proton Synchrotron Booster (PSB) at CERN. During the experiment in 2015, a fresh bunch of protons were incident on the production target at ISOLDE every whole multiple of 1.2 seconds. A clock in the DAQ was constantly running during the experiment and was reset every time the production of ^{21}Mg commenced. The current reading of the clock was in turn recorded for every trigger generated by the detectors of the setup. In figure 6.4 all clock readings coinciding with one or more events in the 60 µm–500 µm telescope of the setup are depicted against the corresponding proton energies in the telescope. The horizontal discontinuities in the figure are due to the 1200 millisecond repitition cycle of the PSB. For energies above 1800 keV the exponential decay of ^{21}Mg is evident: The number of simultaneously existing precursors reach a peak within the vacuum chamber around 200 to 400 milliseconds after the clock is reset and then diminish in numbers over a series of half-lives, $t_{1/2} \simeq 120$ ms. The time after production being less than 1500 milliseconds is in fact also a constraint which is utilised in the production of figure 6.3. Below 1800 keV the signals drown in background; the situation is, unsurprisingly, even more grave for a similar plot of clock readings against the energies recorded in the Clover detectors. Rather

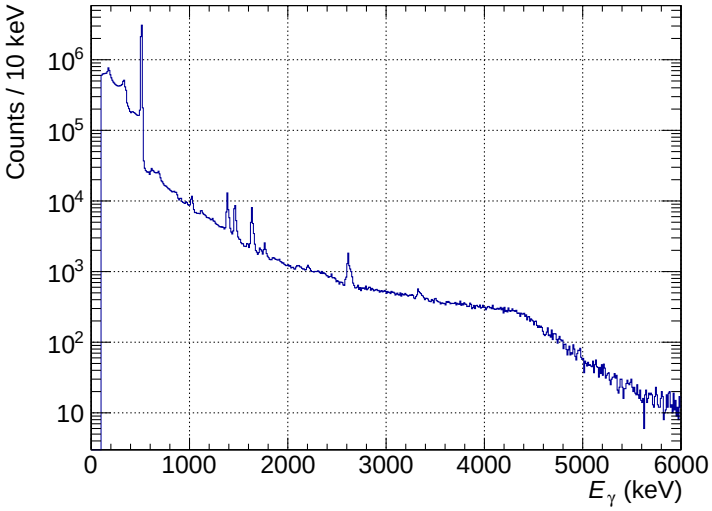

Figure 6.5: Gamma spectrum of all Clover detectors of the setup, including addback but with no further constraints.

than showing this, a one-dimensional spectrum of all Clover detectors is instead depicted in figure 6.5; the amount of background in the spectrum is evident, but some of the peaks can still be attributed to the decay of ^{21}Mg: The 1634 keV line, the 2614 keV line and the 3333 keV line, for example, all stem from the deexcitation of ^{20}Ne. In the next section I will demonstrate some relations of these energy levels to the distribution of proton energies.

6.2 Preliminary results

Before relating the observed protons and photons to each other, there are, however, some things worth noting back in figure 6.3. The extreme dip in the spectrum around $E_{\mathrm{cm}} = 2.3$ MeV between the peaks at $E_{\mathrm{cm}} = 2.0$ MeV and 2.6 MeV is indicative of destructive interference between the levels in this area. Other less intense levels also seem to be present. Much physics insight lies here, as the interference of two levels implies shared quantum properties of the levels; knowing the properties of one level, the properties of the other level can be deduced. Going much further than this, utilising the *R-matrix framework* [27], proper energies, widths and β-strength parameters for the resonances concerned can be extracted. Another noteworthy feature in figure 6.3 is the area between roughly $E_{\mathrm{cm}} = 5.2$ MeV and 6.0 MeV, which

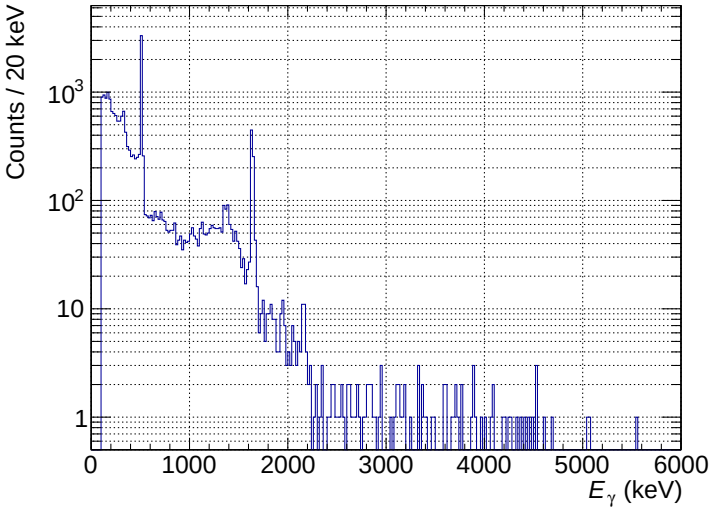

Figure 6.6: Gamma spectrum with a gate on $E_{\mathrm{cm}} = 4.9$ MeV in figure 6.3.

also reveals nuclear structure. This area has previously been studied mainly through (p, p) and (p, γ) reactions, and the features of some of the levels are poorly known. A further investigation of this part of the spectrum should also be rewarding.

Now, by gating on the most intense $E_{\mathrm{cm}} = 4.9$ MeV peak in figure 6.3, keeping active the constraints already imposed, the gamma spectrum of figure 6.6 emerges. Compared to the gamma spectrum of figure 6.5 there is a tremendous reduction in the overall background, both from annihilation photons, bremsstrahlung, etc. and also from the gamma lines originating from background radiation. Especially the 1634 keV transition from the 2^+ excited state to the 0^+ ground state in ^{20}Ne is present; referring back to the decay scheme in figure 6.1, this is consistent with a proton being emitted from the IAS in ^{21}Na, populating the 2^+ state in ^{20}Ne. The spectrum also retains some of the broader gamma line around 1380 keV – this is a fiendish one. The line could be indicative of a less intense population of the 4^- state in ^{20}Ne, which would primarily deexcite through a 1383 keV transition to the 3^- state, then to the 2^+ state, and finally to the ground state of ^{20}Ne. The transition from the IAS in ^{21}Mg to the 4^- state in ^{20}Ne is, however, not kinematically possible, so the presence of this transition would be indicative of a highly excited contamination of ^{20}Ne. The β-decay of ^{214}Bi in the decay chain

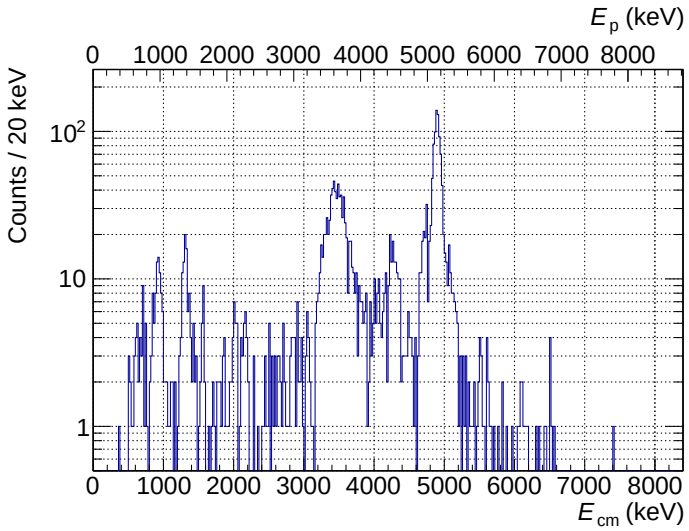

Figure 6.7: Proton spectrum with a gate on $E_\gamma = 1634$ keV in figure 6.5.

of ^{226}Ra could also contribute a contaminant gamma line of 1385 keV, but a plot similar to the one in figure 6.4 with E_γ instead of E_p along the abscissa reveals the same characteristic exponential decay in this area of gamma energies. The explanation for the presence of this line is merely, referring to the decay scheme in figure 6.1, the deexcitation of the 1.7 MeV state to the 0.3 MeV state in ^{21}Na, below the threshold for proton emission. This is, however, a good example of the care one must employ in these kinds of deductions.

Gating instead on the 1634 keV gamma line in figure 6.5, utilising also the constraints leading to figure 6.3, results in the proton spectrum of figure 6.7. First of all, this serves as a check on the $E_{cm} = 4.9$ MeV IAS peak of the previous gate. However, several other levels are also present in this spectrum. The second and third most prominent peaks in the spectrum around $E_{cm} = 3.5$ MeV and 4.3 MeV can only be due to the feeding of states in ^{21}Na of energies lower than the IAS, both due to the fact that the gate is specifically on the feeding of the 2^+ state in ^{20}Ne (this state could of course also be populated via a cascade from higher-lying levels), but most of all because no known level transitions in ^{20}Ne would be consistent with protons of these energies being emitted from the IAS. There are clearly a lot of details on nuclear structure to be revealed in spectra produced by these kinds of gates on observed proton and gamma energies. Through the application of more of

these gates and by their combination, the known decay scheme of ^{21}Mg can be checked and unknown apsects of the decay scheme can be unravelled.

7 Outlook

My plan with regard to my PhD project, from this point onward, is to continue and condense the analysis of ^{21}Mg, thus preparing myself for the analyses to be carried out on the data from MSU *and* consolidating and expanding upon the current knowledge of the β-delayed decay of ^{21}Mg. In carrying out this work, I also intend to expand my analytical toolkit, e.g. with the R-matrix framework which I briefly alluded to in the previous section. R-matrix theory is relevant as soon as broad and/or close-lying levels are present in the spectra under study; this was seen to be the case in the previous section, and it will definitely also be the case for the nuclides to be studied at MSU.

In addition to extending the analysis of ^{21}Mg to the new data on ^{22}Al, ^{26}P, ^{23}Si and ^{27}S from MSU, there is also the possibility of applying the same techniques to other relevant data, which are already available to the Subatomic Group; data on ^{31}Ar and ^{17}Ne, for example. There will inevitably be experiment-specific details to account for, but otherwise the same methods should be applicable. This all fits my intention of maintaining, further future-proofing and expanding upon the Subatomic Group's analytical toolkit, as I progress in my analyses of this rich array of neutron-deficient nuclei.

Bibliography

[1] Vittorio Somà. "From the liquid drop model to lattice QCD: A brief history of nuclear interactions." In: *Eur. Phys. J. Plus* 133.10 (2018), p. 434. DOI: 10.1140/epjp/i2018-12244-2.

[2] E. A. M. Jensen. *AUSA / Erik / nuchart*. GitLab — Aarhus University. 2021. URL: https://gitlab.au.dk/ausa/erik/nuchart (visited on 06/29/2021).

[3] W. J. Huang et al. "The AME2016 atomic mass evaluation (I). Evaluation of input data; and adjustment procedures." In: *Chinese Phys. C* 41.3 (Mar. 2017), p. 030002. DOI: 10.1088/1674-1137/41/3/030002.

[4] M. Wang et al. "The AME2016 atomic mass evaluation (II). Tables, graphs and references." In: *Chinese Phys. C* 41.3 (Mar. 2017), p. 030003. DOI: 10.1088/1674-1137/41/3/030003.

[5] G. Audi, F. G. Kondev, M. Wang, W. J. Huang, and S. Naimi. "The NUBASE2016 evaluation of nuclear properties." In: *Chinese Phys. C* 41.3 (Mar. 2017), p. 030001. DOI: 10.1088/1674-1137/41/3/030001.

[6] AMDC: Atomic Mass Data Collaboration. *ATOMIC MASS DATA CENTER*. 2017. URL: http://amdc.impcas.ac.cn (visited on 06/29/2021).

[7] Beam experts at MSU. Private communication. 2018-2021.

[8] B. Blank and M. J. G. Borge. "Nuclear structure at the proton drip line: Advances with nuclear decay studies." In: *Prog. Part. Nucl. Phys.* 60.2 (Apr. 2008), pp. 403–483. DOI: 10.1016/j.ppnp.2007.12.001.

[9] M. Pfützner, M. Karny, L. V. Grigorenko, and K. Riisager. "Radioactive decays at limits of nuclear stability." In: *Rev. Mod. Phys.* 84 (2 Apr. 2012), pp. 567–619. DOI: 10.1103/RevModPhys.84.567.

[10] K. S. Krane. *Introductory Nuclear Physics*. 3rd ed. Wiley, Oct. 1987. ISBN: 978-0471805533.

[11] R. Bennett et al. *Radioactive Nuclear Beam Facilities*. Apr. 2000. URL: http://nupecc.org/pub/radioactive_nuclear_beam_facilities_2000.pdf (visited on 07/07/2021).

[12] Micron Semiconductor Ltd. *Silicon Detector Catalogue | Micron Semiconductor Ltd.* 2018. URL: http://micronsemiconductor.co.uk/silicon-detector-catalogue (visited on 06/28/2021).

[13] O. Tengblad, U. C. Bergmann, L. M. Fraile, H. O. U. Fynbo, and S. Walsh. "Novel thin window design for a large-area silicon strip detector." In: *Nucl. Instrum. Meth. A* 525.3 (2004), pp. 458–464. ISSN: 0168-9002. DOI: 10.1016/j.nima.2004.01.082.

[14] W. F. Mueller, J. A. Church, and P. Quirin. "Thirty-two-fold segmented germanium detectors to identify γ-rays from intermediate-energy exotic beams." In: *Nucl. Instrum. Meth. Phys. Res. A* 466.3 (July 2001), pp. 492–498. DOI: 10.1016/S0168-9002(01)00257-1.

[15] M. K. Munch, O. S. Kirsebom, J. H. Jensen, A. Gad, and E. A. M. Jensen. *AUSA / AUSAlib*. GitLab — Aarhus University. 2021. URL: https://gitlab.au.dk/ausalib (visited on 07/02/2021).

[16] R. Brun and F. Rademakers. "ROOT: An object oriented data analysis framework." In: *Nucl. Instrum. Meth. A* 389 (1997), pp. 81–86. DOI: 10.1016/S0168-9002(97)00048-X.

[17] ROOT Team. *ROOT 7 - ROOT*. 2021. URL: https://root.cern/for_developers/root7 (visited on 07/11/2021).

[18] Kitware, Inc. and Contributors. *CMake*. 2021. URL: https://cmake.org (visited on 07/12/2021).

[19] Kitware, Inc. and Contributors. *CMake 3.19 Release Notes — CMake 3.19.8 Documentation*. 2020. URL: https://cmake.org/cmake/help/v3.19/release/3.19.html (visited on 07/11/2021).

[20] pkgs.org - Packages Search for Linux and Unix operating systems. *Cmake Download (APK, DEB, EOPKG, RPM, TGZ, TXZ, XZ, ZST)*. 2021. URL: https://pkgs.org/download/cmake (visited on 07/12/2021).

[21] D. Pfeiffer. *Effective CMake*. Presentation. 2017. URL: https://cppnow2017.sched.com/event/A8J6/effective-cmake (visited on 07/12/2021).

[22] R. Bast and R. Di Remigio. *CMake Cookbook*. Packt Publishing, Sept. 2018. ISBN: 978-1788470711.

[23] E. A. M. Jensen. *AUSA / Erik / AUSAlib2021*. GitLab — Aarhus University. 2021. URL: https://gitlab.au.dk/ausa/erik/ausalib2021 (visited on 07/05/2021).

[24] M. V. Lund et al. "Beta-delayed proton emission from ^{21}Mg." In: *Eur. Phys. J. A* 51.9 (June 2015), p. 113. DOI: 10.1140/epja/i2015-15113-1.

[25] S. T. Nielsen. "An experimental study of the decay of ^{21}Mg." MA thesis. Department of Physics and Astronomy, Nov. 2016. URL: https://wiki.kern.phys.au.dk/thesisSTN.pdf.

[26] R. Lică. "Development of the ISOLDE Decay Station and ɣ spectroscopic studies of exotic nuclei near the N=20 "Island of Inversion"." PhD thesis. CERN, Oct. 2017. URL: https://cds.cern.ch/record/2292847.

[27] A. M. Lane and R. G. Thomas. "R-Matrix Theory of Nuclear Reactions." In: *Rev. Mod. Phys.* 30 (2 Apr. 1958), pp. 257–353. DOI: 10.1103/RevModPhys.30.257.